Journal of Materials Chemistry A

Spray-Drying Synthesis and Vanadium-Catalyzed Graphitization of a Nanocrystalline γ-$Li_{3.2}V_{0.8}Si_{0.2}O_4$/C Anode Material with a Unique Double Capsule Structure

Journal:	*Journal of Materials Chemistry A*
Manuscript ID	TA-ART-10-2022-007825.R1
Article Type:	Paper
Date Submitted by the Author:	30-Nov-2022

Complete List of Authors:	Matsumura, Keisuke; Tokyo University of Agriculture and Technology, Department of Applied Chemistry Iwama, Etsuro; Tokyo University of Agriculture and Technology, Department of Applied Chemistry; Tokyo University of Agriculture and Technology, Global Innovation Research Organization; Tokyo University of Agriculture and Technology, Advanced Capacitor Research Center Takagi, Kenta; Tokyo University of Agriculture and Technology, Department of Applied Chemistry Hashizume, Naoki; Tokyo University of Agriculture and Technology, Department of Applied Chemistry Chikaoka, Yu; Tokyo University of Agriculture and Technology, Department of Applied Chemistry; Tokyo University of Agriculture and Technology, Global Innovation Research Organization Okita, Naohisa; Tokyo University of Agriculture and Technology, Department of Applied Chemistry Naoi, Wako; K & W Inc. Naoi, Katsuhiko; Tokyo University of Agriculture and Technology, Department of Applied Chemistry; Tokyo University of Agriculture and Technology, Global Innovation Research Organization; Tokyo University of Agriculture and Technology, Advanced Capacitor Research Center

ARTICLE

Spray-Drying Synthesis and Vanadium-Catalyzed Graphitization of a Nanocrystalline γ-$Li_{3.2}V_{0.8}Si_{0.2}O_4$/C Anode Material with a Unique Double Capsule Structure

Received 00th January 20xx,
Accepted 00th January 20xx

DOI: 10.1039/x0xx00000x

Keisuke Matsumura[a], Etsuro Iwama*[abc], Kenta Takagi[a], Naoki Hashizume[a], Yu Chikaoka[ab], Naohisa Okita[a], Wako Naoi[d], and Katsuhiko Naoi*[abc]

By means of a simple spray-drying method, a unique double capsule structure of nanocrystalline lithium superionic conductor (LISICON)-type γ-$Li_{3.2}V_{0.8}Si_{0.2}O_4$ (γ-LVSiO) has first been obtained for anodes of hybrid supercapacitors. The synthetic procedure involves simultaneous carbonization on crystals which brings about fine control of morphologies of the whole entity of composites depending upon some critical conditions like dispersion diluteness and sucrose concentration as a carbon source. Fine control of those parameters brings about the highest possible rate performance with minimal carbon content without sacrificing the specific energy density of the electrode materials. A significantly efficient network of electrons/ions is constructed across the interphase of embedded γ-LVSiO nanoparticles (ϕ = 50 nm) whereby vanadium (IV) catalytically induced graphitization selectively in the vicinity of nano-γ-LVSiO surfaces: such graphitization occurs at surprisingly low temperature (700 °C); the graphitization normally occurs at over 1000 °C as elsewhere reported. The authors revealed an unexpectedly efficient interconnection of two different carbons, *viz.*, graphitic and amorphous carbons formed by this method. Such a unique dual-carbon network facilitates an excellent rate performance of γ-LVSiO with a modest total carbon content (12.4 wt%) within γ-LVSiO composites. A vanadium-based 0.4-mAh-class full cell consisting of this γ-LVSiO anode and $Li_3V_2(PO_4)_3$ cathode has been assembled for any possible availability as future hybrid supercapacitors or high-power superbatteries. In fact, the cell exhibited outstandingly fast-discharging performance, maintaining 50% of capacity at 100C rate, and no capacity degradation during 10C/10C cycle test with a long-term cycling over 1000 cycles.

Introduction

Electric double-layer capacitors (EDLCs) are electrochemical energy storage devices that operate using the charge mechanism of ions physically adsorbing to the electrode surface [1]. Owing to their simple operating mechanism, EDLCs exhibit high power densities, long cyclabilities, and low resistances. Thus, EDLCs have been used for power-assist or highly efficient energy regeneration [2]. However, because the charge is stored only at the surface of the electrodes, EDLCs generally have low energy densities. Designing hybrid supercapacitors by combining activated carbon (AC) cathodes and faradaic (battery-like) anode materials, or even superbatteries combining two ultrafast pseudocapacitive or battery materials can overcome the energy density limitation of conventional EDLCs because of their redox reaction [3, 4]. The hybrid supercapacitors need an anode that can respond to the fast non-faradaic reaction of the cathode. Various anode materials have been explored: carbon-based materials, such as graphite and hard carbon [5]; metal oxides, such as TiO_2 [6], $Li_4Ti_5O_{12}$ (LTO) [7-9], Nb_2O_5 [10], and $TiNb_2O_7$ [11]; other insertion-type layered materials, such as MXene [12, 13]; metal-organic frameworks [14, 15]; and conversion or alloy-type materials, such as Si [16], Sn [17], and TiS_2 [18]. Only two of these, *i.e.*, graphite and LTO, have been commercialized as batteries and hybrid supercapacitors. Graphite is commonly used in commercial lithium-ion hybrid supercapacitors; however, it faces the risk of lithium dendrite deposition because of its low reaction potential [5]. LTO is also employed because of its high-power density and long cyclability, resulting from its zero-strain reaction mechanism. However, LTO delivers a high reaction potential of 1.55 V *vs.* Li/Li^+ and a small specific capacity of 175 mAh g^{-1}, sacrificing the energy density of the full cell [19]. Therefore, alternative anode materials are highly desirable for designing cells with safety, high energy and power densities, and long cyclability.

γ-Phase $Li_{3+x}V_{1-x}Si_xO_4$ (γ-LVSiO) has a theoretical capacity of 287–377 mAh g^{-1} (x=0.05–0.3, based on V^{3+}/V^{5+}) and a reaction potential of 0.4–1.3 V *vs.* Li/Li^+, which can achieve a high cell voltage and an energy density exceeding that of LTO (175 mAh g^{-1}) with its sufficient potential margin to the risk of lithium dendrite deposition [20, 21]. The Si substitution of V in β-phase

[a] Department of Applied Chemistry, Tokyo University of Agriculture & Technology, 2-24-16 Naka-cho, Koganei, Tokyo 184-8558, Japan. E-mail: iwama@cc.tuat.ac.jp (E.I.), k-naoi@cc.tuat.ac.jp (K.N.)
[b] Global Innovation Research Organization, Tokyo University of Agriculture & Technology, 2-24-16 Naka-cho, Koganei, Tokyo, 184-8588, Japan
[c] Advanced Capacitor Research Center, Tokyo University of Agriculture & Technology, 2-24-16 Naka-cho, Koganei, Tokyo 184-8558, Japan
[d] Division of Art and Innovative Technologies, K & W Inc., 1-3-16-901 Higashi, Kunitachi, Tokyo 186-0002, Japan
† Electronic Supplementary Information (ESI) available:
See DOI: 10.1039/x0xx00000x

Li_3VO_4 (β-LVO) results in the stabilization of the high-temperature phase (> 700 °C) of LVO, called the γ-phase, at room temperature [21]. γ-LVSiO shows a higher Li^+ conductivity (10^{-7}–10^{-5} S cm^{-1}) [22, 23] than β-LVO (10^{-12}–10^{-10} S cm^{-1}) [23-25] owing to its lithium superionic conductor (LISICON)-like crystal structure[22, 23, 26]. The Li^+ conductivity of γ-LVSiO is expected to be further improved based on the doping strategy studied for LISICON-based solid electrolytes [25]. Another advantage of γ-LVSiO is its reversible electrochemical profiles from the 1st cycle compared to that of β-phase LVO, which undergoes irreversible profile change during initial cycling due to the cation-disordering between Li^+ and V^{5+} [20, 21]. However, γ-LVSiO and β-LVO have poor electronic conductivity (10^{-7}–10^{-6} S m^{-1}) [20]. Considerable research has been focused on solving such intrinsic issues, involving particle down-sizing [27], morphological approaches (hollow spheres [28-32], nanofibers [33-37], and nanoparticles [38-40]), carbon coating [41-47], and the use of carbon composites, such as LVO/graphene [48-51], LVO/reduced graphene oxide [52-55], LVO/carbon nanowires [56], and LVO/multiwalled carbon nanotubes [57-59]. Especially, spray dry-assisted routes for carbon-coating or compositing with conductive agents have been reported to be effective in terms of scalability and uniformity [38, 53, 55, 58, 60, 61]. Large-scale spray dryers can synthesize several tons of material per hour under precise morphological control. However, as previously reported for β-phase LVO/C [60, 61], the conventional spray-drying method provides a hollow shell structure, which is composed of nanoparticles but with low density, sacrificing its energy density. This morphological drawback is due to the nature of the feed solution.

Herein, we firstly synthesized the high ionic phase of γ-$Li_{3.2}V_{0.8}Si_{0.2}O_4$ carbon composites by a simple spray drying method, whereby a fine control of the dispersion diluteness of γ-LVSiO, highly dense morphology can be obtained without excessive aggregation. The synthesized γ-LVSiO/C were found to have a unique capsule-like structure with a 200-nm-thick outer shell filled with carbon-coated γ-LVSiO nanoparticles of *ca.* 50 nm in diameter. The carbon formed a continuous network of graphitized carbon on the surface of γ-LVSiO and amorphous carbon, fulfilling the inter-particles. Morphological and physicochemical characterization of γ-LVSiO/C was carried out using electron microscopy and X-ray diffraction. The amount of carbon and graphitization ratio were quantified by thermogravimetry (TG) and Raman spectroscopy. The catalytic effect of vanadium on the formation mechanism of both graphitic and amorphous carbon was investigated by comparing V and P in γ-$Li_{3.2}M_{0.8}Si_{0.2}O_4$ (M= P and V). Furthermore, we elucidated the electrochemical contribution of the unique nano-capsule structure and dual-carbon network of amorphous and graphitic carbon, leading to exceptional electrochemical properties without the extra addition of conductive agents. These findings of the spray drying-assisted route for vanadium-based compounds offer a strategy for the mass production of effective carbon-composited materials for energy-storage devices.

Experimental methods

Materials

Li_2CO_3 (99%, FUJIFILM Wako Pure Chemical Co.), V_2O_5 (99%, FUJIFILM Wako Pure Chemical Co.), and SiO_2 (99%, FUJIFILM Wako Pure Chemical Co.) were used to prepare a γ-LVSiO powder. To synthesize the γ-$Li_{3.2}P_{0.8}Si_{0.2}O_4$ (γ-LPSiO) powder, $(NH_4)_2HPO_4$ (99%, Kanto Chemical Co.) was used in place of V_2O_5. Sucrose (99%, FUJIFILM Wako Pure Chemical Co.) was used as the carbon source.

Preparation of the γ-LVSiO and γ-LPSiO powder samples

γ-LVSiO powder was synthesized *via* a simple solid-state reaction method as follows: First, 2.4694 g (0.8 eq.) of V_2O_5, 4.2135 g (3.2 eq. + 5 wt%) of Li_2CO_3, and 0.4079 g (0.2 eq.) SiO_2 powder were ground using a planetary ball mill machine (Planetary Micro Mill, Pulverisette 7 premium line: PL-7, Fritsch) at 300 rpm for 30 min (dry ball-milling process). Notably, an excess amount (5 wt%) of Li_2CO_3 was always added to the objective stoichiometry to offset the volatile loss of Li. Second, the obtained mixture was preheated to 600 °C for 5 h and then calcined at 900 °C for 8 h in a standard electric furnace (FO100, Yamato Scientific Co., Ltd.) to obtain γ-LVSiO powder. γ-LPSiO powder was synthesized using the same procedure; a mixture of 4.0773 g (0.8 eq.) of $(NH_4)_2HPO_4$, 4.7907 g (3.2 eq. + 5 wt%) of Li_2CO_3, and 0.4637 g (0.2 eq.) of SiO_2 were ball-milled calcined to obtain γ-LPSiO powder.

Preparation of the γ-LVSiO/C and γ-LPSiO/C composites

Capsule-like γ-LVSiO/C composites were synthesized by a spray-drying process as follows: first, the synthesized γ-LVSiO powder (1 g) was pulverized by wet ball-milling (PL-7) with ethanol (7 mL) at 800 rpm for 10 min. Afterward, the samples were dried overnight at 80 °C under vacuum to remove most of the solvent. The dried γ-LVSiO powder and different amounts of sucrose (10–50 wt%) were dispersed in deionized water (10.00 g L^{-1}). Then, the white dispersion was spray-dried using a mini spray drier (B-290, BUCHI), where the inlet temperature, dry air flow (aspirator rate), sample feed flow, and the atomizing gas of N_2 flow were set to 160 °C, 38 m^3 h^{-1}, 7.5 mL min^{-1}, and 473 L h^{-1}, respectively. Capsule-like γ-LVSiO/C composites were obtained after carbonization of the sucrose contained in the spray-dried composite precursor at 700 °C for 5 h under N_2 gas flow in an infrared furnace (SSA-P610CP, ADVANCE RIKO, Inc.). γ-LPSiO/C composites were also prepared *via* the same spray-drying process as the γ-LVSiO/C composite.

Physicochemical characterization of the capsule-like γ-LVSiO/C

Phase identification and structural analysis of the synthesized capsule-like γ-LVSiO/C were conducted using X-ray diffraction techniques. (Rigaku MiniFlex600, Cu Kα radiation, λ = 1.54056 Å; operating at 40 kV and 15 mA). The XRD patterns were recorded in the 2θ range of 10–80° with a step rate of 2.0° min^{-1}. The morphology and elemental distribution of the capsule-like γ-LVSiO/C composites were characterized using a combination of scanning electron microscopy and energy-

dispersive X-ray spectroscopy (SEM-EDX, Hitachi S-5500). The nanostructures of the particles inside the capsule were characterized using scanning transmission electron microscopy (Hitachi, HD-2700). TG measurements were performed in synthetic air (20% O_2, 80% N_2) using a thermogravimetric and differential thermal analyzer with photography equipment (Hitachi, STA200RV). The Raman spectra of γ-LVSiO/C were recorded on a HORIBA LabRAM HR Evolution Raman spectrometer. The specific surface area was obtained from N_2 adsorption-desorption isotherms (BELSORP-max, Bel Japan, Inc.).

Electrochemical characterization of the capsule-like γ-LVSiO/C

The 2032-type coin cells were assembled using γ-LVSiO/C (cathode) and Li metal (anode) electrodes. The cathode was prepared by mixing the γ-LVSiO/C composite with sodium carboxymethyl cellulose and styrene-butadiene rubber (CMC/SBR) in a 95:2.5:2.5 mass ratio in deionized water; no conducting additives were used. The mixture was coated on a Cu foil and dried at 80 °C under vacuum for 12 h. The electrodes were 19–21 μm thick with a weight loading in the range of 1.8–2.4 mg cm^{-2}. The electrolyte used was a 1.0 M solution of lithium hexafluorophosphate ($LiPF_6$) in a 1:1 (by volume) mixture of ethylene carbonate (EC) and diethyl carbonate (DEC), supplied by Kishida Chemicals (water content <50 ppm). One layer of 25-μm-thick polypropylene film (Celgard2400) was used as the separator. The electrochemical performance was evaluated between 0.1 and 2.5 V *vs.* Li/Li^+ under constant current mode at various current densities ranging from 0.1 to 10 A g^{-1} (HJ-SD8, Hokuto Denko Corp.). The electrodes for studying the effect of graphitic carbon were prepared by mixing active materials with single-wall carbon nanotubes (0.2 wt%, TUBALL™, OCSiAl) as conductive agents with a large aspect ratio. To demonstrate the rate-capability and cyclability of full cells based on the γ-LVSiO/C, the 0.4-mAh-class laminate-type cells were assembled by combining γ-LVSiO/C anode and $Li_3V_2(PO_4)_3$ (LVP)/multiwalled carbon nanotube (MWCNT) cathode. Here, $Li_3V_2(PO_4)_3$ (LVP)/MWCNT was selected as a cathode material due to its excellent rate-capability and cyclability, as previously reported. The electrolyte composition was 1 M $LiBF_4$/EC+DEC (1:1 by volume). Prior to any full cell cycling, Li^+ pre-doping using Li metal was conducted as previously reported [62]. Briefly, the γ-LVSiO/C anode was charged in the constant–current constant–voltage (CC–CV) mode with a cut-off potential of 0.6 V *vs.* Li/Li^+ and a holding time of 1 h. Then, the cell was opened to remove the Li metal electrode, and then sealed. Both the laminated and coin-type cells were assembled in a dry room (dew-point temperature below −40 °C). Electrochemical impedance spectroscopy (EIS) was performed on the symmetric laminate-type cells composed of two identical γ-LVSiO/C electrodes (5 cm^2). EIS measurements were carried out at OCV [fully discharged state: state of charge (SOC) = 0%] using a perturbation signal of ±10 mV within a frequency range from 10 mHz to 1 MHz.

Results and discussion

Preparation of the capsule-like carbon composite of γ-LVSiO

A unique double capsule structured composites of LVSiO/C were synthesized through solid-state reaction (synthesis of (a) γ-LVSiO), ball-milling of LVSiO ((b) pulverized γ-LVSiO), and subsequent spray drying/carbonization processes ((c) γ-LVSiO/carbon composites) as shown in Figure 1. The crystalline structure with a space group *Pnma* and its chemical compositions of γ-phase $Li_{3.2}V_{0.8}Si_{0.2}O_4$ remained intact after the spray drying/ carbonization process, confirmed by XRD analysis (Figure 1), and inductively coupled plasma mass spectrometry measurements, respectively. XANES and EXAFS profiles of powders obtained from V K-edge XAFS experiments (Figure S1) support that the valence number of V^{5+} and V–O radial distance did not change during the synthesis process. Note that all XRD peaks were found at lower 2θ angles compared to the reference patterns, because of the difference in atomic compositions (samples: $Li_{3.2}V_{0.8}Si_{0.2}O_4$ and the reference: $Li_{3.6}V_{0.4}Si_{0.6}O_4$). Apparent average crystallite sizes of γ-LVSiO calculated from the Scherrer equation using full width at half maximum (FWHM) of 200, 020, and 002 peaks were tabulated in Table S1. The calculated crystallite size for the samples as-synthesized (after solid-state calcination), after ball-milling, and spray dry/carbonization processes, respectively. The γ-LVSiO crystallite size after spray dry/carbonization processes were 120, 70, and 50 nm, respectively. Interestingly, the crystallite size after spray dry/carbonization processes was 30% smaller compared to that after ball-milling despite the carbonization process at 700 °C, possibly inducing particle growth. Such reduction in crystallite size indicates a partial dissolution of γ-LVSiO in the aqueous feed solution, which is analogue to previously reported "water-etching of LVO" [32, 63]. High-resolution SEM observation confirms the unique macro/nanostructure of the obtained γ-LVSiO/C samples. Figure 2a clearly shows a spherical structure of the composites (diameter 0.1–5 μm) specific to spray-dried samples where the atomized droplets form spheres due to surface tension as reported anywhere for the spray-drying process. In a cross-sectional image of the sphere (Figure 2b), a unique capsule structure involving an outer-shell and densely packed inner-particles can be found as illustrated in 3D-fashion, unlike the previously reported spray-dried LVO samples, which only have a hollow shell structure [60]. Magnified SEM image (Figure 2c) and its traced image (Figure 2d) reveal the detailed morphology of inner particles and the outer shell. The diameter of uniform-sized inner nanoparticles was *ca.* 50 nm, well agreeing with the calculated average crystallite size. Despite its outlook of being densely packed, the inner nanoparticles were loosely interconnected, as depicted in the schematics of Figure 2. EDS elemental mapping of the cross-sectional view of the γ-LVSiO/C capsule (Figure S2) shows that the C atoms, as well as other atoms (V, Si, O), are uniformly distributed through all over the composites. Such well-dispersed carbon may play a role as a buffer to prevent the growth of crystallite size (50 nm) during the carbonization process at 700 °C for 5 h.

To elucidate the formation mechanism of the unique double capsule structure of γ-LVSiO, two different types of feed solutions were spray-dried: i) an aqueous solution containing dissolved Li, V, and Si resources to be 1 wt% of γ-LVSiO after calcination as well as sucrose (30 wt%), and ii) concentrated dispersions containing 10 wt% of γ-LVSiO ball-milled powders and 30 wt% of sucrose. As shown in SEM images of Figure S3, distinctly different morphologies were obtained from two feed solutions. Using the feed solution i), only a thin densified shell structure was obtained (Figure S3a), while huge aggregates of γ-LVSiO particles without shell were obtained from the feed solution ii). The contrasting results obtained from two feed solutions indicate that the peculiar double-capsule structure of the γ-LVSiO/C was formed via the spray drying process where two different drying mechanisms simultaneously proceeded [64]. The important key is the low concentration of the used feed solution containing only 1 wt % of the solid-phase (ball-milled γ-LVSiO particles), which can be regarded as "ultra-dilute" compared to solid content applied for conventional spray-drying processes [65-68]. As discussed in the above section (see XRD analysis in Figure 1 and Table S1), the γ-LVSiO particles partially dissolved in the aqueous feed solution, resulting in a mixture of ionized compounds such as Li^+, $H_xVO_4^{(3-x)-}$, and $H_xSiO_4^{(4-x)-}$, whose existence was identified by NMR spectroscopy (Figure S4). In the ultra-dilute feed solution, such ionized precursors slurry of γ-LVSiO, as well as the γ-LVSiO solid content, may have a major impact on the obtained composite morphology after spray-drying. Considering those facts, two-way agglomerate/granulate-building mechanisms with instant water evaporation dynamics were postulated in Figure 3. As illustrated in Figure 3a, an initial stage of a droplet as sprayed (*ca.*10^{-6} s after ejection [69]) forms the nozzle typically spherical-shaped ultra-dilute aqueous slurry/dispersion. The droplets contain γ-LVSiO solid grains of 1 wt%, as well as liquid-phase ionized γ-LVSiO elements. Approximately 10^{-2} s after ejection [69], the droplets are then subjected to hot-dried N_2 spiral turbulence at a temperature of 160 °C, which instantly evaporates water from the droplets (Figure 3b). Such vaporization of droplets induces the constant flow of water outwards (indicated as blue arrows in Figure 3b). These flow dynamics carry the liquid-phase precursors to the droplet surfaces due to capillary action [70, 71] (indicated as black arrows in Figure $3b_1$). Then, the gradually condensed liquid-phase γ-LVSiO precursors build shell-shaped granules. Such a condensation/aggregation mechanism finally leads to the formation of a thick solid OUTER SHELL. On the other hand, the solid-phase γ-LVSiO nanoparticles experience a strong inward cohesive force (indicated as grey arrows in Figure $3b_2$), letting the particles get together to build a core which resulted in aggregated INNER PARTICLE. This aggregated structure is possibly controlled by the dispersion diluteness of the original feed solution; thus, 1 wt% of the γ-LVSiO-solid concentration may suppress excessive aggregation (Figure S3). From the above, the double capsule structure (Figure 2), which has two distinct characteristics of the core/shell architecture in their structures, is considered as thus formed by the two-way drying processes of the droplets with solid grains of γ-LVSiO and liquid phase of the γ-LVSiO precursor. It should be noted that such fine control of morphology by the spray drying process is simply possible by preparing an unconventionally dilute dispersion as a feed solution and is universally applicable to any other nanomaterials synthesis.

To quantify the amounts of carbons derived from sucrose, thermogravimetric (TG) analysis was performed on γ-LVSiO/C. The obtained TG curve is shown in Figure 4a. A slight weight loss (< 1wt%) observed at temperatures below 200 °C can be attributed to the removal of adsorbed water. Above 200 °C, apparent weight loss can be found in the two temperature ranges of 250–450 °C (Region I: 7.9 wt%) and 600–850 °C (Region II: 2.6 wt%), corresponding to the combustion of amorphous and graphitic carbon, respectively [72]. The obtained results were supported by another TG analysis on two different carbons of graphite and Ketjen Black (KB) in the absence of γ-LVSiO. As shown in Figure 8, TG weight losses for KB and graphite were observed around 650 °C and 750 °C, respectively. The results demonstrate that the combustion temperature of carbon increases with an increment of the sp^2 characteristics of carbons (KB < graphite). The fact that Region II (600–850 °C) lies between KB and graphite indicates that the TG loss in Region II would correspond to the combustion of a partially ordered graphitic carbon phase. As shown in Figure 4b, high-resolution STEM images combined with EDS elemental mapping visualizes a homogeneous distribution of the carbon species around γ-LVSiO nanoparticles where V, Si, and O atoms (see also Figure S5) are present. The overlapped carbon and vanadium elemental mapping clearly highlights the interconnected carbon network, which completely fills the interstices between γ-LVSiO nanoparticles. The magnified bright-field STEM images of the γ-LVSiO display where the amorphous and graphitic carbons are surrounding the γ-LVSiO nanoparticles. As shown in Figure 5 (upper), non-crystalline amorphous carbon can be observed in the interstices of the γ-LVSiO nanocrystals with typical *d*-spacings of 2.7 ((400) plane) and 4.1 Å ((210) plane), suggesting that the amorphous carbon plays the main role in the formation of interconnected carbon network. Focusing on the surface of the γ-LVSiO nanocrystals (Figure 5 (lower)), a partially ordered phase of graphitic carbon with 2–4 stacked layers can be observed. The measured interlayer distance of the graphitic carbon was *ca.* 3.6 Å, which is similar to those for graphene nanosheets or carbon nanotubes (3.6–4.0 Å), rather than that for perfectly ordered graphite (3.34 Å) [73]. As shown in the schematics of the γ-LVSiO/C composite (right in Figure 5), the sphere-shaped γ-LVSiO/C composites (ϕ = 0.1–5 μm) have the specific double capsule architecture. The combination of sp^2 graphitic carbon layers (1–2 nm in thickness) on the γ-LVSiO crystal surface and the amorphous carbon between the crystal interstices (10–100 nm in length) may provide efficient electronic conduction, which is discussed in the later section of this manuscript. Besides, the 200-nm-thick outer shell was composed of the aggregated hollow γ-LVSiO nanoparticles (ϕ = 20–50 nm), which includes numerous voids in the structure and thus may enable an electrolyte infiltration through the shell (Figure S6).

V-derived catalytic graphitization mechanism of carbon

The observed 2-4 stacks of graphene layers in the STEM image (Figure 5) indicate that the sucrose on the surfaces of the γ-LVSiO nanocrystals was catalytically graphitized, as the applied carbonization temperature in this study (700 °C) is relatively low compared to the commonly reported temperatures (> 1000 °C) [74]. The fact that the TG curve for the carbonized sucrose in the absence of γ-LVSiO shows only Region I corresponding to the amorphous carbon (Figure S8) supports the hypothesis. As reported in previous studies, it is known that certain vanadium alloys and oxides act as a catalyst for graphitization [74-76]. Thus, it is no wonder that the vanadium in γ-LVSiO catalytically graphitized the sucrose in the vicinity of its nanoparticle surface.

To verify such catalytic graphitization effect of vanadium in γ-LVSiO, comparisons were made between γ-LVSiO/C and its analogue compound γ-$Li_{3.2}P_{0.8}Si_{0.2}O_4$ /C (γ-LPSiO/C), which was synthesized by using exactly the same spray drying method as γ-LVSiO except for the presence of P^{5+} instead of the V^{5+}. The XRD pattern of the γ-LPSiO was indexed to the space group *Pnma*, the same as γ-LVSiO (Figure S9), and no impurity peaks were observed. All the peaks of γ-LPSiO were shifted to higher 2θ angles than those of γ-LVSiO, well agreeing with a smaller ionic radius [77] of P^{5+} (0.17 Å) compared to that of V^{5+} (0.36 Å). The obtained results suggest the successful substitution of the 3*d* metal ion V^{5+} in γ-LVSiO by $P^{5+,}$ which has no electrons in 3*d* orbital. The γ-LPSiO powder was then dispersed in a sucrose solution, and the dispersion was spray-dried/carbonized to obtain γ-LPSiO/C. The obtained TG curve for γ-LPSiO/C is displayed in Figure 6a alongside γ-LVSiO/C and shows only one clear weight loss in Region I corresponding to amorphous carbon combustion. The recorded images of the two samples at three different temperatures of 30, 500, and 800 °C from TG measurements are shown in Figure 6b. While both powder samples were black in color at 30 °C, the color difference became obvious at higher temperatures. At 500 °C, where all the amorphous carbon was combusted, γ-LVSiO/C still remained black because of the presence of graphitic carbon, while γ-LPSiO/C turned into clear white. The γ-LVSiO/C finally changed into white at 800 °C, where all graphitic carbon was burned off. Above 800 °C, shrinkage of the whole sample structure was observed, indicating the collapse of the microcapsule structure due to the sintering of nanoparticles without the carbon coating (see the supporting movie1). Furthermore, Raman spectroscopy was performed at the same three temperatures as image recording in order to identify the dominant carbon species in the two samples. Using obtained Raman spectra shown in Figure 6c, the intensity ratios of the D-band (defect band of graphite, 1350 cm^{-1}) and G-band (graphite band, 1590 cm^{-1}) peaks (I_D/I_G ratio) were calculated as tabulated in Table 1. At 30 °C, both samples show similar Raman spectra with I_D/I_G ratios close to 1, which corresponds to the value reported for amorphous carbons [78]. The obtained I_D/I_G ratio for the γ-LVSiO /C well agrees with the TG analysis and microscopic observation where the amorphous carbon was a major component (7.6 wt%) and in the presence between the γ-LVSiO particles compared to the graphitic carbon (2.6 wt%) existing only on the γ-LVSiO surface. After the combustion of the amorphous carbon at 500 °C, the intensity of the Raman spectra drastically decreased for the γ-LPSiO/C, where only 0.2 wt% of residual ash compounds remained. For γ-LVSiO/C, the I_D/I_G ratio decreased to 0.448, which agrees well with the presence of residual graphitic carbon [79]. At 800 °C, Raman spectra for D- and G-bands totally disappeared, while those for the γ-LVSiO and γ-LPSiO can still be observed. Those results demonstrate that the formation mechanism of graphitic carbon in γ-LVSiO/C was attributed to the catalytic effect of vanadium.

Table 1. The I_D/I_G ratios of γ-LVSiO/C and γ-LPSiO/C at three different temperatures; before heating up (30 °C), after combustion of the amorphous carbon (500 °C), and graphitic carbon (800 °C).

Sample	I_D/I_G ratio		
	30 °C	500 °C	800 °C
γ-LPSiO/C	0.935	1.960	-
γ-LVSiO/C	0.980	0.448	-

To further elucidate the mechanism of vanadium-induced catalytical carbon formation, XPS measurements were conducted for the γ-LVSiO/C and γ-LPSiO/C. As shown in Figure S10, the clear peak attributed to C–O or C=O bonds around 289 eV can be found only for the γ-LVSiO/C, while its intensity is negligible for the γ-LPSiO/C. The results indicate the existence of the chemical interaction between the carbon and oxygen atoms of the γ-LVSiO crystal surface, such as C–O–V bonds, as shown in Figure S11. The formation of C–O–V bonds may initiate the nucleation of carbon species, resulting in an arrangement of a carbon layer along the surface profile of γ-LVSiO crystals. Such arranged carbon layer on the γ-LVSiO crystals surface induces a few (2-4 layers) of carbon layer stacking to form the graphitic carbon. Additionally, the electron spin resonance (ESR) spectra were measured for the γ-LVSiO/C to evaluate the oxidation state of vanadium. As shown in Figure S12a, the presence of V^{4+} was detected for the spray-dried powder of the γ-LVSiO/C precursors before carbonization. After the carbonization process (Figure S12b), the V^{4+} was clearly diminished. Thus, it is considered that the *d*-electron of V^{4+} may back-donate to the antibonding π^* orbitals of C=C, thereby improving the affinity between V^{4+} and the sp^2 carbon. This stabilization effect between the sp^2 carbon and the γ-LVSiO surface lowered the activation energy, resulting in the catalytic graphitization at the low temperature of 700 °C.

Electrochemical characterization of the spray-dried γ-LVSiO/C

To differentiate the contribution of the graphitic and amorphous carbons to the electrochemical performance, γ-LVSiO/C composites with various ratios of graphitic/amorphous carbons were synthesized using different dosages of sucrose in feed solution containing 1 wt% of ball-milled γ-LVSiO particles. As shown in Figure S13, all XRD patterns of the γ-LVSiO/C samples with 0–50 wt% sucrose (denoted as Suc. 0, 10, 20, 30,

40, 50 wt%) were indexed to the γ-LVSiO structure without any impurity, which is indicative of successful synthesis of γ-LVSiO/C regardless of the sucrose dosage. The broadness of XRD peaks was found to be function with values of sucrose dosage, indicating the dependence of the crystallite sizes on the amount of carbon formed around γ-LVSiO particles. The calculated crystallite sizes from the FWHM of three representative XRD peaks corresponding to 200, 020, and 002 reflections and their averages are tabulated in Table S2. After a slight increase from Suc. 0 to Suc. 10 wt%, the average crystallite size continuously decreased with an increase of sucrose dosage up to 30 wt% (Suc. 30 wt%), while that became more or less constant over 30 wt%. These results suggest that the particle growth during annealing at 700 °C was inhibited by carbonized sucrose, and the 30 wt% dosage was enough to cover almost all the surfaces of the 1 wt % of ball-milled γ-LVSiO particles. TG analysis was conducted on six samples to estimate the weight content of obtained amorphous and graphitic carbons within γ-LVSiO/C compounds (Figure 7). As shown in the TG curves of Figure 7a, the sucrose dosage makes a clear difference in the weight loss of the Region I (250–450 °C; amorphous carbon). Accordingly, the estimated amount of amorphous carbon from the TG loss in Region I proportionally increased with an increase in sucrose dosage, as plotted in Figure 7b. Unlike the Region I, little change in TG weight loss was observed in the Region II (600–850 °C; graphitic carbon) regardless of sucrose dosage. The resultant amount of graphitic carbon was almost constant between 2.1 and 3.8 wt%, although the highest value (3.8 wt%) was obtained for Suc. 20wt%. Such an almost constant value indicates that the amount of graphitic carbon formed within γ-LVSiO/C largely depends on the surface area of γ-LVSiO particles, well agreeing with the proposed formation mechanism where the sucrose is catalytically graphitized in the vicinity of the γ-LVSiO surface. As depicted in Figure 5, the amorphous carbon formed within γ-LVSiO/C is to fill the interstices between γ-LVSiO particles, and thus may play an important role for the electric connection between γ-LVSiO particles.

To elucidate the correlation between the amount of amorphous carbon and electrochemical performances, rate performance tests were performed on Li metal half cells using γ-LVSiO/C. Figure S14 shows representative charge-discharge profiles of γ-LVSiO/C (Suc. 30 wt%) at 0.1 A g^{-1} during the initial 20 cycles. A reversible pseudocapacitive slope observed in 0.4–1.3 V *vs.* Li/Li^+ corresponds to the reversible 2-electron redox reaction of V^{3+}/V^{5+} in γ-LVSiO [20, 21]. The curve can be divided into two regions; i) a sloping reaction region at 0.5–1.0 V *vs.* Li/Li^+ corresponding to the redox of V^{4+}/V^{3+} and ii) a plateau-like region at 1.0–1.5 V *vs.* Li/Li^+ corresponding to the redox of V^{5+}/V^{4+}. An irreversible plateau observed around 0.7 V *vs.* Li/Li^+ at the initial cycle corresponds to the reductive decomposition of electrolyte [80]. The exhibited capacities for five γ-LVSiO/C samples (Suc. 10–50 wt%) at different C-rates (0.1 and 10 A g^{-1}) were plotted in Figure 8 to see the correlation between their electrochemical performances and the amount of sucrose-derived amorphous carbons. At a low C-rate of 0.1 A g^{-1}, exhibited capacity drastically increased with an increase of the sucrose dosage over 20 wt% (Suc. 20 wt%). The obtained capacity of Suc. 30 wt% reached 288 mAh g^{-1} (composite), which corresponds to 103% of its theoretical capacity (279 mAh g^{-1}) considering the 20% Si^{4+} substitution of active V^{5+} and the presence of 12.5 wt% of carbon in total. By increasing the sucrose dosage up to 50 wt%, the capacity gradually decreased but still showed a high capacity of 230 mAh g^{-1}. At a high C-rate of 10 A g^{-1}, the capacity was maximized for Suc. 30 wt%, then drastically decreased to 100 and then 50 mAh g^{-1} for Suc. 40 and 50 wt%, respectively. Focusing on the charge curves (inset of Figure 8), the curve shapes for Suc. 40–50 wt% became steeper at 10 A g^{-1} compared to those at a slow rate of 0.1 A g^{-1}, indicating the large diffusion overpotential due to the excess amount of amorphous carbon (13.4–17.8 wt%). On the other hand, the curve of Suc. 10 wt% with little amount of amorphous carbon (2.47 wt%) did not exhibit any capacity due to the large IR drop over 3 V (see also enlarged curves in Figure S16), even at a low current density of 0.1 A g^{-1}. Such large IR drop for the Suc. 10 wt% indicates lack of electronic connections between γ-LVSiO particles. These results highlight the importance of optimizing amorphous carbon to have balanced electric and ion paths.

To further discuss the role of amorphous carbon on the resistances of γ-LVSiO/C composites, EIS measurements using a symmetric blocking cell were performed for Suc. 10, 30, and 50 wt%, which represent the typical cases of insufficient (2.5 wt%), optimal (9.5 wt%), and excess (19.2 wt%) amorphous carbons, respectively. As shown in Figure 9, EIS spectra for the Suc. 10 wt% show a huge semicircle of over 300 kΩ cm^2 attributed to the electronic resistance of grain boundary (R_e). For Suc. 30 wt% with an increase of amorphous carbon, the R_e drastically decreased to 0.358 Ω cm^2. The R_e for Suc. 50 wt% re-increased to 13.6 Ω cm^2, probably due to the γ-LVSiO crystals surface being covered with a slightly less amount of graphitic carbon and excess of less-electron-conductive amorphous carbon compared to that of Suc. 30 wt%. Ionic resistances (R_{ion}), which is a characteristic of electrolyte diffusion within composite matrix were estimated from the slope in the spectra at a middle frequency [81] assuming their knee frequency as 10^3 Hz. The estimated R_{ion}s for Suc. 30 and 50 wt% were 16.2 and 106 Ω cm^2, respectively, which are significantly larger than R_e (> 8–45 times), indicating that R_{ion} is the dominant factor in the total resistance of the two γ-LVSiO/C composites. Such digit increases of R_{ion} from Suc. 30 to 50 wt% may well explain the inferior rate performance for Suc. 50 wt% compared to that for Suc. 30 wt%, as discussed in Figure 8. The dependence of R_{ion} on the amount of amorphous carbon was further supported by nitrogen adsorption-desorption measurements for Suc. 10, 30, and 50 wt%. As shown in Figure S16a, the isotherm for Suc. 50 wt% can be categorized into a type II with small but clear hysteresis compared to those for Suc. 10 and 30 wt%, indicating the development of micro/mesopores within the composite. In fact, the estimated Brunauer-Emmett-Teller (BET) specific surface area of Suc. 50 wt% was 24.0 m^2 g^{-1}, which was the largest among the three samples (6.8 and 4.4 m^2 g^{-1} for Suc. 10 and 30 wt%, respectively). However, derived Barrett-Joyner-Halenda (BJH) plots for Suc. 50 wt% (see the inset of Figure S16a) shows the pore distribution only below 10 nm, while pores larger than

10 nm can be clearly recognized in pore distributions for the other two compounds. Thus, it can be considered that the excess of amorphous carbon for Suc. 50 wt% (19.2 wt%) fills such beyond-10-nm pores, resulting in an increase of R_{ion} due to the interference in ionic diffusion toward the surface of γ-LVSiO crystals, as illustrated in Figure S16b. It should be noted that the BET specific surface area for Suc. 30 wt%, 4.4 m^2 g^{-1}, corresponds to the 1/30 of the previously reported LVO hollow sphere (128.6 m^2 g^{-1}) [60] synthesized *via* the spray-drying method, further supporting the dense morphology observed in the SEM images (Figure 2).

Further, the contribution of the graphitic carbon on the surface of γ-LVSiO was demonstrated by comparing two model samples: the Suc. 0 wt% without any carbon content and Suc. 10 wt%, which contains 2.3 wt% of graphitic and insufficient amount (2.5 wt%) of amorphous carbons. To focus on the electrochemical contribution of the graphitic carbon in the vicinity of the γ-LVSiO surface, the electron conduction between γ-LVSiO particles was ensured by adding 0.2 wt% of single-walled carbon nanotubes (SWCNTs) with over 5-μm length. As summarized in Figure S17, the exhibited capacity at 0.1 A g^{-1} was 216.5 mAh g^{-1}, 1.6 times as high as that for Suc. 0 wt%. Even at higher current densities up to 10 A g^{-1}, the capacities for Suc. 10 wt% overwhelmed those for Suc. 0 wt%, showing that the graphitic carbon imparts the electron conduction to the surface of γ-LVSiO particles as depicted in Figure S17a and b.

Finally, vanadium-based 0.4-mAh-class full cells were assembled by combining an optimized γ-LVSiO/C composite anode (Suc. 30 wt%) with a $Li_3V_2(PO_4)_3$ (LVP) cathode. We used LVP materials synthesized *via* a unique ultracentrifugation (uc) technique [82]. The uc-treated LVP contains highly crystalline LVP nanoparticles (diameter = 10–100 nm), which are highly dispersed within a MWCNT matrix. The uc-LVP/MWCNT composites enabled a high C-rate operation of 96 mAh g^{-1} at 300 C and excellent cycle performance over 10,000 cycles. Prior to the full cell cycling, the operation voltage (2.1–3.5 V) is optimized/controlled by Li^+ pre-dope (Figure 10a), as previously reported [62]. The obtained charge discharge curves in the inset of Figure 10b typically reflect the combined characteristics of charge-discharge profiles of two electrodes: the slope of γ-LVSiO/C and inflection points at approximately 3.60, 3.65, and 4.05 V vs. Li/Li^+ due to the three-step plateaus of uc-LVP/MWCNT (Figure S18). The Suc. 30 wt%//uc-$Li_3V_2(PO_4)_3$/MWCNT full cell showed no capacity degradation and no charge-discharge curve distortion during 10C/10C cycling after 1000 cycles (Figure 10b). As shown in Figures 10c and d, the assembled Suc. 30 wt%//uc-LVP/MWCNT full cell showed excellent rate capability; approximately 50% of capacity retention was maintained even at high rates of 30C (charge) and 100C (discharge). As shown in Ragone plots (Figure S19), the γ-LVSiO//LVP full cell exhibited the high energy density of 180 Wh kg^{-1} at 1C-rate based on mass of anode material, which significantly surpassed the energy density of supercapacitors (AC//AC) [83] and hybrid capacitors such as LTO//AC[83,84] and LVO//AC[56, 85]. Those energy values of γ-LVSiO//LVP are relatively smaller than those of LVO-based-batteries[41, 61]; however, our γ-LVSiO//LVP exhibited ultrafast performance equivalent to 400C-rate (discharge in 0.9 s), and high energy density of 100 Wh kg^{-1} was maintained at ultrahigh power density of 10 kW kg^{-1}, which significantly outperformed other studies. Such excellent performances of the Suc. 30 wt%//uc-$Li_3V_2(PO_4)_3$/MWCNT full cell demonstrates promising characteristics of Suc. 30 wt% as an anode material for ultrafast electrochemical energy devices (hybrid capacitors and superbatteries) with long cycle lives.

Conclusions

Unique double-capsule structured composites of γ-phase $Li_{3.2}V_{0.8}Si_{0.2}O_4$ (γ-LVSiO) nanocrystals embedded in the continuous carbon network were successfully synthesized by spray drying and subsequent annealing of the feed solution containing 1 wt% of γ-LVSiO solid particles with 30 wt% of sucrose aqueous solution as a carbon source. Obtained γ-LVSiO/C composites had high crystallinity identified as a lithium superionic conductor (LISICON)-type structure. From the SEM observations, we found its specific morphology where 50-nm uniform inner particles of γ-LVSiO were encapsulated within densified 200-nm-thick outer shell, which was also constituted with hollow nano-γ-LVSiO particles. The important key to synthesize such unique core/shell architecture was the ultra-dilute condition of feed solution with only 1 wt% of the solid-phase γ-LVSiO. HR-STEM observation and TG measurements identified composited carbon species as the two phases of amorphous/graphitic carbon. The surface of the γ-LVSiO nanoparticles was uniformly coated with the graphitic carbon (1–2 nm in thickness), which imparted the electron conduction to the γ-LVSiO surface and improved the utilization of γ-LVSiO in the electrode. The graphitic carbon was selectively formed in the vicinity of the γ-LVSiO surface due to the catalytic effect of V^{4+}, which was demonstrated by comparing the γ-$Li_{3.2}P_{0.8}Si_{0.2}O_4$ without any graphitic carbon formation. In contrast, the amorphous carbon fulfilled the interstices among the γ-LVSiO nanoparticles, which formed the continuously connected network as the middle-distance of electron conduction (10–100 nm in length). Further, it was clarified that the amorphous carbon content strongly correlated to the rate performance for the γ-LVSiO. Excess amount of the amorphous carbon (> 14 wt%) filled the pores in the composite and increased the overpotential for electrolyte diffusion, while the shortage of the carbon (< 5 wt%) caused disconnection of the electronic pathways. By optimizing the total carbon content (12.4 wt%) with sucrose dosage of 30 wt% in the feed solution, the γ-LVSiO/C composites exhibited the excellent rate performance (199 mAh g^{-1} at 10 A g^{-1}) without extra addition of conductive agents due to the exceptional electronic and ionic conduction of the dual-carbon structure. Finally, the vanadium-based 0.4-mAh-class full cell, which was assembled by combining an γ-LVSiO/C anode with a $Li_3V_2(PO_4)_3$/multi-walled carbon nanotubes cathode, exhibited the fast-discharging performance, maintaining 50% of capacity at 100C rate, and no capacity degradation during 10C/10C cycling after 1000 cycles.

Author Contributions

Conceptualization: KM, EI, KN. Data curation: KM, EI, KT, NH. Formal Analysis: KM, KT, NH. Funding acquisition: EI, KN. Investigation: KM, EI, KT, NH, YC, NO, WN. Methodology: KM, KT, NH, YC, NO, WN. Project administration: EI, KN. Resources: EI, KN. Supervision: EI, KN. Validation: KT, NH. Visualization: KM, WN, KN. Writing – original draft: KM, EI, KN. Writing – review & editing: EI, KN.

Conflicts of interest

There are no conflicts to declare.

Acknowledgements

This study was supported by the Global Innovation Research Organization in TUAT, JSPS Grant-in-Aid for Scientific Research (KAKENHI) A under Grant No. JP19H00882, KAKENHI C under Grant No. JP21K05241, and the Adaptable and Seamless Technology Transfer Program through Target-Driven R&D from Japan Science and Technology Agency (A-STEP; AS282S002d). The synchrotron radiation experiments were performed at the BL01B1 of SPring-8 with the approval of the Japan Synchrotron Radiation Research Institute (JASRI) (Proposal No. 2018A1528 and 2019A1607).

References

1. P. Simon and Y. Gogotsi, *Nature Materials*, 2020, **19**, 1151-1163.
2. M. Salanne, B. Rotenberg, K. Naoi, K. Kaneko, P. L. Taberna, C. P. Grey, B. Dunn and P. Simon, *Nature Energy*, 2016, **1**, 1-10.
3. C. Choi, D. S. Ashby, D. M. Butts, R. H. DeBlock, Q. Wei, J. Lau and B. Dunn, *Nature Reviews Materials*, 2019, **5**, 5-19.
4. P. X. Han, G. J. Xu, X. Q. Han, J. W. Zhao, X. H. Zhou and G. L. Cui, *Advanced Energy Materials*, 2018, **8**, 1801243-1801243.
5. P. Jezowski, O. Crosnier, E. Deunf, P. Poizot, F. Beguin and T. Brousse, *Nature Materials*, 2018, **17**, 167-173.
6. K. Naoi, T. Kurita, M. Abe, T. Furuhashi, Y. Abe, K. Okazaki, J. Miyamoto, E. Iwama, S. Aoyagi, W. Naoi and P. Simon, *Adv. Mater.*, 2016, **28**, 6751-6757.
7. E. Zhao, C. Qin, H. R. Jung, G. Berdichevsky, A. Nese, S. Marder and G. Yushin, *Acs Nano*, 2016, **10**, 3977-3984.
8. K. Naoi, W. Naoi, S. Aoyagi, J. Miyamoto and T. Kamino, *Acc. Chem. Res.*, 2013, **46**, 1075-1083.
9. T. F. Yi, S. Y. Yang and Y. Xie, *Journal of Materials Chemistry A*, 2015, **3**, 5750-5777.
10. V. Augustyn, J. Come, M. A. Lowe, J. W. Kim, P. L. Taberna, S. H. Tolbert, H. D. Abruna, P. Simon and B. Dunn, *Nature Materials*, 2013, **12**, 518-522.
11. Y. Li, Y. Wang, R. Cai, C. Yu, J. Zhang, J. Wu, C. S. Tiwary, J. Cui, Y. Zhang and Y. Wu, *J. Colloid Interface Sci.*, 2022, **610**, 385-394.
12. X. Zhang, L. Wang, W. Liu, C. Li, K. Wang and Y. Ma, *Acs Omega*, 2020, **5**, 75-82.
13. Q. Z. Zhu, J. P. Li, P. Simon and B. Xu, *Energy Storage Materials*, 2021, **35**, 630-660.
14. N. Ogihara, N. Ohba and Y. Kishida, *Science Advances*, 2017, **3**, e1603103.
15. R. Mikita, N. Ogihara, N. Takahashi, S. Kosaka and N. Isomura, *Chem. Mater.*, 2020, **32**, 3396-3404.
16. Y. B. An, S. Chen, M. M. Zou, L. B. Geng, X. Z. Sun, X. Zhang, K. Wang and Y. W. Ma, *Rare Metals*, 2019, **38**, 1113-1123.
17. F. Sun, J. Gao, Y. Zhu, X. Pi, L. Wang, X. Liu and Y. Qin, *Scientific Reports*, 2017, **7**, 40990.
18. L. Zhang, D. Sun, J. Kang, H. T. Wang, S. H. Hsieh, W. F. Pong, H. A. Bechtel, J. Feng, L. W. Wang, E. J. Cairns and J. H. Guo, *Nano Lett.*, 2018, **18**, 4506-4515.
19. T. Yuan, Z. P. Tan, C. R. Ma, J. H. Yang, Z. F. Ma and S. Y. Zheng, *Advanced Energy Materials*, 2017, **7**, 1601625-1601625.
20. G. Liang, L. Yang, Q. Han, G. Chen, C. Lin, Y. Chen, L. Luo, X. Liu, Y. Li and R. Che, *Advanced Energy Materials*, 2020, **10**, 1904267.
21. C. Liao, Y. Wen, Z. Xia, R. Qin, X. Liu, Y. Yu, B. Shan, T. Zhai and H. Li, *Advanced Energy Materials*, 2018, **8**, 1701621.
22. A. Khorassani and A. R. West, *J. Solid State Chem.*, 1984, **53**, 369-375.
23. G. Zhao, K. Suzuki, T. Seki, X. Sun, M. Hirayama and R. Kanno, *J. Solid State Chem.*, 2020, **292**, 121651.
24. A. R. Rodger, J. Kuwano and A. R. West, *Solid State Ionics*, 1985, **15**, 185-198.
25. S. Muy, J. C. Bachman, H. H. Chang, L. Giordano, F. Maglia, S. Lupart, P. Lamp, W. G. Zeier and Y. Shao-Horn, *Chem. Mater.*, 2018, **30**, 5573-5582.
26. H. Y. P. Hong, *Mater. Res. Bull.*, 1978, **13**, 117-124.
27. M. X. Zhang, X. Zhang, Z. X. Liu, H. F. Peng and G. K. Wang, *Ionics*, 2020, **26**, 4129-4140.
28. C. K. Zhang, C. F. Liu, X. H. Nan, H. Q. Song, Y. G. Liu, C. P. Zhang and G. Z. Cao, *Acs Applied Materials & Interfaces*, 2016, **8**, 680-688.
29. Y. Shi, J. Z. Wang, S. L. Chou, D. Wexler, H. J. Li, K. Ozawa, H. K. Liu and Y. P. Wu, *Nano Lett.*, 2013, **13**, 4715-4720.
30. Y. Shi, J. Gao, H. D. Abruna, H. J. Li, H. K. Liu, D. Wexler, J. Z. Wang and Y. P. Wu, *Chemistry-a European Journal*, 2014, **20**, 5608-5612.
31. Q. D. Li, Q. L. Wei, Q. Q. Wang, W. Luo, Q. Y. An, Y. A. Xu, C. J. Niu, C. J. Tang and L. Q. Mai, *Journal of Materials Chemistry A*, 2015, **3**, 18839-18842.
32. Q. D. Li, J. Z. Sheng, Q. L. Wei, Q. Y. An, X. J. Wei, P. F. Zhang and L. Q. Mai, *Nanoscale*, 2014, **6**, 11072-11077.
33. Z. Xu, D. B. Li, J. Xu, J. L. Lu, D. M. Zhang and S. B. Ni, *Electrochim. Acta*, 2021, **384**, 138386.
34. D. B. Li, Z. Xu, D. M. Zhang and S. B. Ni, *Ionics*, 2021, **27**, 4705-4712.
35. Z. Xu, D. M. Zhang, J. L. Lu, C. Y. Pei, T. Li, T. Xiao and S. B. Ni, *Journal of Materials Chemistry A*, 2021, **9**, 24002-24011.
36. R. H. Qin, G. Q. Shao, J. X. Hou, Z. Zheng, T. Y. Zhai and H. Q. Li, *Science Bulletin*, 2017, **62**, 1081-1088.
37. Z. Xu, J. L. Lu, D. B. Li, D. M. Zhang, D. Z. Yang and S. B. Ni, *J. Alloys Compd.*, 2022, **893**, 162178.
38. J. N. Ye, J. X. Cheng, W. Q. Xiao, L. Xi, F. Xie and Y. J. Hu, *New J. Chem.*, 2018, **42**, 13241-13248.
39. X. N. Xu, F. E. Niu, C. S. Wang, Y. J. Li, C. L. Zhao, J. Yang and Y. T. Qian, *Chem. Eng. J.*, 2019, **370**, 606-613.
40. D. Zhao and M. H. Cao, *Acs Applied Materials & Interfaces*, 2015, **7**, 25084-25093.
41. L. F. Shen, S. Q. Chen, J. Maier and Y. Yu, *Adv. Mater.*, 2017, **29**, 1701571.
42. G. Q. Shao, L. Gan, Y. Ma, H. Q. Li and T. Y. Zhai, *Journal of Materials Chemistry A*, 2015, **3**, 11253-11260.

43. X. T. Wang, B. Qin, D. Sui, Z. H. Sun, Y. Zhou, H. T. Zhang and Y. S. Chen, *Energy Technology*, 2018, **6**, 2074-2081.
44. Z. Y. Liang, Y. M. Zhao, Y. Z. Dong, Q. Kuang, X. H. Lin, X. D. Liu and D. L. Yan, *J. Electroanal. Chem.*, 2015, **745**, 1-7.
45. Z. Y. Liang, Z. P. Lin, Y. M. Zhao, Y. Z. Dong, Q. Kuang, X. H. Lin, X. D. Liu and D. L. Yan, *J. Power Sources*, 2015, **274**, 345-354.
46. H. Park, W. Jae and J. Kim, *J. Alloys Compd.*, 2018, **767**, 657-665.
47. Z. Y. Liang, Y. M. Zhao, L. Z. Ouyang, Y. Z. Dong, Q. Kuang, X. H. Lin, X. D. Liu and L. Yan, *J. Power Sources*, 2014, **252**, 244-247.
48. Z. L. Jian, M. B. Zheng, Y. L. Liang, X. X. Zhang, S. Gheytani, Y. C. Lan, Y. Shi and Y. Yao, *Chem. Commun.*, 2015, **51**, 229-231.
49. S. B. Ni, J. C. Zhang, J. J. Ma, X. L. Yang and L. L. Zhang, *J. Power Sources*, 2015, **296**, 377-382.
50. M. X. Zhang, L. Dong, C. W. Zhang, F. X. Yin, H. F. Peng and G. K. Wang, *J. Power Sources*, 2020, **468**, 228364.
51. M. X. Zhang, R. J. Bai, S. King, F. X. Yin, H. F. Peng and G. K. Wang, *Energy Storage Materials*, 2021, **43**, 482-491.
52. Q. D. Li, Q. L. Wei, J. Z. Sheng, M. Y. Yan, L. Zhou, W. Luo, R. M. Sun and L. Q. Mai, *Advanced Science*, 2015, **2**, 1500284.
53. Y. Yang, J. Q. Li, J. X. Huang, J. X. Huang, J. Zeng and J. B. Zhao, *Electrochim. Acta*, 2017, **247**, 771-778.
54. J. Cao, D. M. Zhang, P. P. Sun, D. Z. Yang and S. B. Ni, *Ionics*, 2021, **27**, 1041-1048.
55. H. C. Liu, P. Hu, Q. Yu, Z. H. Liu, T. Zhu, W. Luo, L. Zhou and L. Q. Mai, *Acs Applied Materials & Interfaces*, 2018, **10**, 23938-23944.
56. L. F. Shen, H. F. Lv, S. Q. Chen, P. Kopold, P. A. van Aken, X. J. Wu, J. Maier and Y. Yu, *Adv. Mater.*, 2017, **29**, 1700142.
57. E. Iwama, N. Kawabata, N. Nishio, K. Kisu, J. Miyamoto, W. Naoi, P. Rozier, P. Simon and K. Naoi, *Acs Nano*, 2016, **10**, 5398-5404.
58. Y. Yang, J. Q. Li, D. Q. Chen and J. B. Zhao, *J. Electrochem. Soc.*, 2017, **164**, A6001-A6006.
59. P. Rozier, E. Iwama, N. Nishio, K. Baba, K. Matsumura, K. Kisu, J. Miyamoto, W. Naoi, Y. Orikasa, P. Simon and K. Naoi, *Chem. Mater.*, 2018, **30**, 4926-4934.
60. Y. Yang, J. Q. Li, X. Y. He, J. Wang, D. Sun and J. B. Zhao, *Journal of Materials Chemistry A*, 2016, **4**, 7165-7168.
61. J. Xu, D. M. Zhang, Z. P. Zhang and S. B. Ni, *Journal of Materials Chemistry A*, 2021, **9**, 10345-10353.
62. Y. Chikaoka, R. Okuda, E. Iwama, M. Kuwao, W. Naoi and K. Naoi, *Electrochemistry*, 2021, **89**, 204-210.
63. J. Xu, P. Liang, D. M. Zhang, C. Y. Pei, Z. P. Zhang, S. Y. Yang and S. B. Ni, *Journal of Materials Chemistry A*, 2021, **9**, 17270-17280.
64. W. J. Jr. Walker, J. S. Reed and S. K. Verma, *J. Am. Ceram. Soc.*, 1999, **82**, 1711-1719.
65. A. Stunda-Zujeva, Z. Irbe and L. Berzina-Cimdina, *Ceram. Int.*, 2017, **43**, 11543-11551.
66. H. Liu, Y. Liu, L. An, X. Zhao, L. Wang and G. Liang, *J. Electrochem. Soc.*, 2017, **164**, A3666-A3672.
67. J. Gao, Z. Huang, J. Li, X. He and C. Jiang, *Ionics*, 2014, **20**, 301-307.
68. C.-W. Chang-Jian, E.-C. Cho, J.-H. Huang, J.-H. Huang, J.-A. Chou, B.-C. Ho, K.-C. Lee and Y.-S. Hsiao, *J. Alloys Compd.*, 2019, **773**, 376-386.
69. D. E. Dobry, D. M. Settell, J. M. Baumann, R. J. Ray, L. J. Graham and R. A. Beyerinck, *Journal of Pharmaceutical Innovation*, 2009, **4**, 133-142.
70. T. Breinlinger, A. Hashibon and T. Kraft, *Powder Technol.*, 2015, **283**, 1-8.
71. T. Mori, H. Imazeki, K. Yamamoto and K. Tsuchiya, *Ceram. Int.*, 2017, **43**, 11170-11176.
72. J. Adelene Nisha, M. Yudasaka, S. Bandow, F. Kokai, K. Takahashi and S. Iijima, *Chem. Phys. Lett.*, 2000, **328**, 381-386.
73. E. Yoo, J. Kim, E. Hosono, H.-s. Zhou, T. Kudo and I. Honma, *Nano Lett.*, 2008, **8**, 2277-2282.
74. A. Ōya and H. Marsh, *Journal of Materials Science*, 1982, **17**, 309-322.
75. L. Tang, Q. Y. Mao, Z. H. You, Z. Yao, X. D. Zhu, Q. F. Zhong and J. Xiao, *Carbon*, 2022, **188**, 336-348.
76. A. Oya and S. Otani, *Carbon*, 1979, **17**, 131-137.
77. R. Shannon, *Acta Crystallographica Section A*, 1976, **32**, 751-767.
78. M. Armandi, B. Bonelli, F. Geobaldo and E. Garrone, *Microporous Mesoporous Mater.*, 2010, **132**, 414-420.
79. O. A. Maslova, M. R. Ammar, G. Guimbretière, J. N. Rouzaud and P. Simon, *Physical Review B*, 2012, **86**, 134205.
80. C. Y. Liao, Y. W. Wen, B. Shan, T. Y. Zhai and H. Q. Li, *J. Power Sources*, 2017, **348**, 48-56.
81. L. L. Zhou, S. Y. Shen, X. X. Peng, L. N. Wu, Q. Wang, C. H. Shen, T. T. Tu, L. Huang, J. T. Li and S. G. Sun, *Acs Applied Materials & Interfaces*, 2016, **8**, 23739-23745.
82. K. Naoi, K. Kisu, E. Iwama, Y. Sato, M. Shinoda, N. Okita and W. Naoi, *J. Electrochem. Soc.*, 2015, **162**, A827-A833.
83. H.-G. Jung, N. Venugopal, B. Scrosati and Y.-K. Sun, *J. Power Sources*, 2013, **221**, 266-271.
84. V. Aravindan, J. Gnanaraj, Y.-S. Lee and S. Madhavi, *Chem. Rev.*, 2014, **114**, 11619-11635.
85. X. N. Xu, F. Niu, D. P. Zhang, C. X. Chu, C. S. Wang, J. Yang and Y. T. Qian, *J. Power Sources*, 2018, **384**, 240-248.

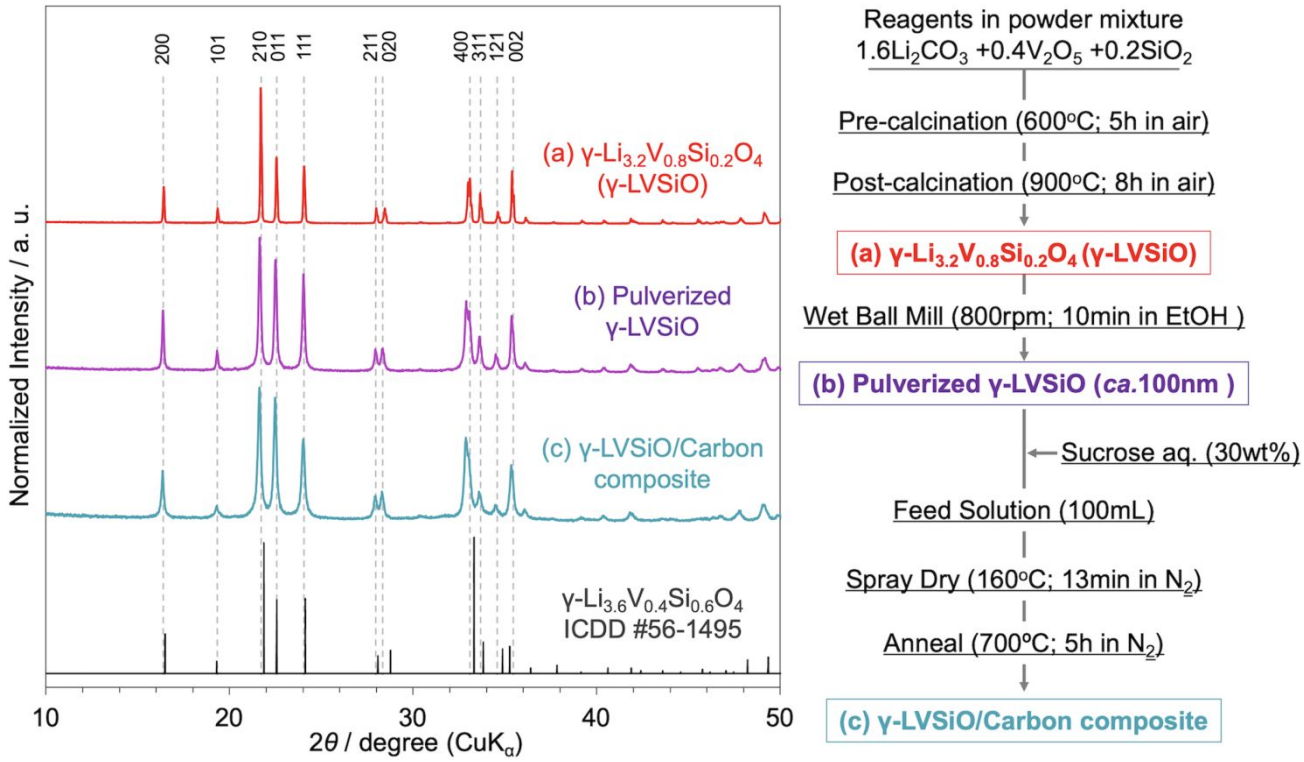

Figure 1. Synthetic flowchart of γ-$Li_{3.2}V_{0.8}Si_{0.2}O_4$/Carbon composites (γ-LVSiO/C) with XRD patterns of resulting γ-LVSiO powders at each step of the procedure. First, reagents in powder mixture (Li_2CO_3 + 0.4V_2O_5 + 0.2SiO_2) were two-step-calcinated to obtain the crystalline (a) γ-LVSiO granules, where pre-calcination was performed to eliminate unevenness of the reagent temperature before crystallization in post-calcination. Then, resulting γ-LVSiO granules were pulverized into (b) nano-powders of γ-LVSiO (ϕ = *ca.* 100 nm) by high-energy wet-ball milling in ethanol solvent. The pulverized γ-LVSiO (1 wt%) were dispersed in sucrose aqueous solution (30 wt%) to prepare feed solution, which was subsequentially spray-dried in dried hot N_2 for a short time (*ca.* 13 min). Obtained dry-γ-LVSiO/Sucrose granules were annealed in N_2 for carbonization, resulting in (c) γ-LVSiO/Carbon composite. All XRD patterns for (a) γ-LVSiO, (b) pulverized γ-LVSiO, and (c) γ-LVSiO/Carbon composite are indexed to the γ-phase structure (space group: *Pnma*) without any impurity peaks, with reference to the pattern of γ-$Li_{3.6}V_{0.4}Si_{0.6}O_4$ from the ICDD database (#56-1495). The shape of the XRD peaks is clearly broadened with progress in the synthetic steps, indicative of downsizing in the crystallite size (tabulated in Table S1).

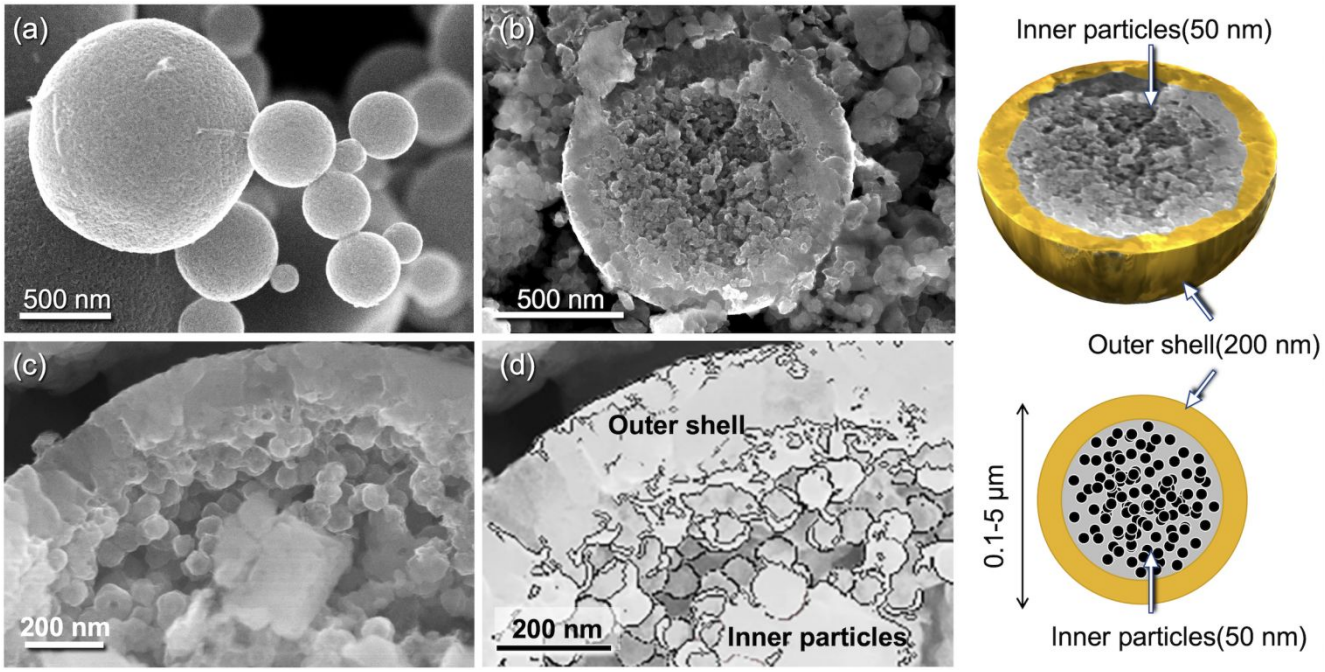

Figure 2. HR-SEM images of the resulting γ-LVSiO-carbon composite (γ-LVSiO/C) powders prepared by spray-dry method from a dilute feed solution containing 1 wt% ball-milled γ-LVSiO pretreated powders and 30 wt% sucrose. Any other conditions are the same throughout entire experiments that are described in the experimental section. (a) The image displays sphere-shaped structure with multiple dimensions ranging from 0.1 to 5 μm in diameter. (b) The cross-sectional image clearly demonstrates the existence of outer shell of 100–200 nm in thickness as illustrated in 3D-fashion. (c) Magnified view of the cross-section of the image of (b) clearly shows thick outer shell as well as many nanoparticles encapsulated in sphere. (d) The trace image emphasizing the size and shapes of the inner particles which displays the uniform dimensions typically 50 nm in diameter

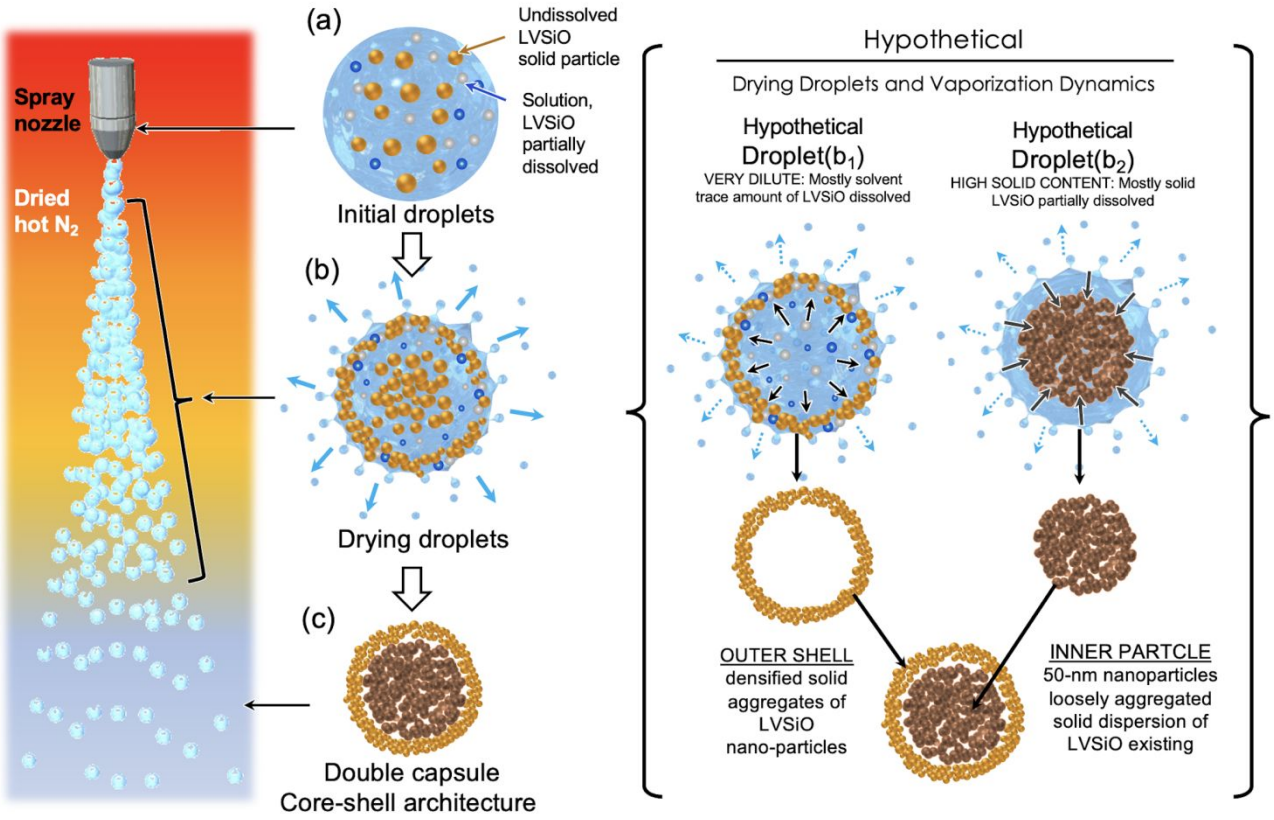

Figure 3. Schematic illustration for the procedure of the spray-dry synthesis of carbonized γ-LVSiO nanoparticles/granules composites. This explains a consecutive water release/vaporization dynamic from sprayed droplets of the original feed solution, which finally resulted in a unique double capsule structure of γ-LVSiO as shown in Figure 2. (a) An initial stage of a droplet as sprayed (more precisely *ca.*10^{-6} s after ejection [69]) forms the nozzle typically spherical-shaped ultra-dilute aqueous slurry/dispersion (due to high surface tension). The constituent of the droplets is pretreated (ball-milled) γ-LVSiO solid grains (1 wt%), as well as a liquid-phase ionized γ-LVSiO elements which are partially dissolved. (b) Approximately 10^{-2} s after ejection [69], the droplets are then subject to hot dried N_2 spiral turbulence at a temperature of 160 °C, which instantly evaporates water from the droplets. (c) About 1 s after ejection [69], peculiar core/shell architecture (indicated in Figure 2) are formed because of the above drying sequence. Such distinct core/shell structure may well be explained by postulating two-way agglomerate/granulate-building mechanisms with instant water evaporation dynamics as suggested below. Two hypothetical droplets (b_1 and b_2) are postulated for basis of the below consideration. The droplet (b_1) contains liquid-phase partially ionized γ-LVSiO precursor slurry of Li^+, $H_xVO_4^{(3-x)-}$, and $H_xSiO_4^{(4-x)-}$ (characterized by NMR, see Figure S4). Vaporization of droplets starts at their surfaces that induces the constant flow of water outwards (indicated as blue arrows). This flow dynamics (indicated as black arrows) due to capillary action makes the precursors gradually condensed at the droplet surfaces to build a shell-shaped granules. Such a condensation/aggregation finally leads to the formation of a thick solid OUTER SHELL. To explain the formation of inner particles, we need to postulate another extreme case namely high solid-content droplet. The droplet (b_2) undergoes different pathway when they are subject to dry. Droplet (b_2) is mostly solid-phase γ-LVSiO nanoparticles that experience a strong inward cohesive force (grey arrows) letting the particles get together to build a core which resulted in aggregated INNER PARTICLE. The double capsule (Figure 2) which has two distinct characteristics in their structures is considered as thus formed by postulating the above drying processes (b_1) and (b_2).

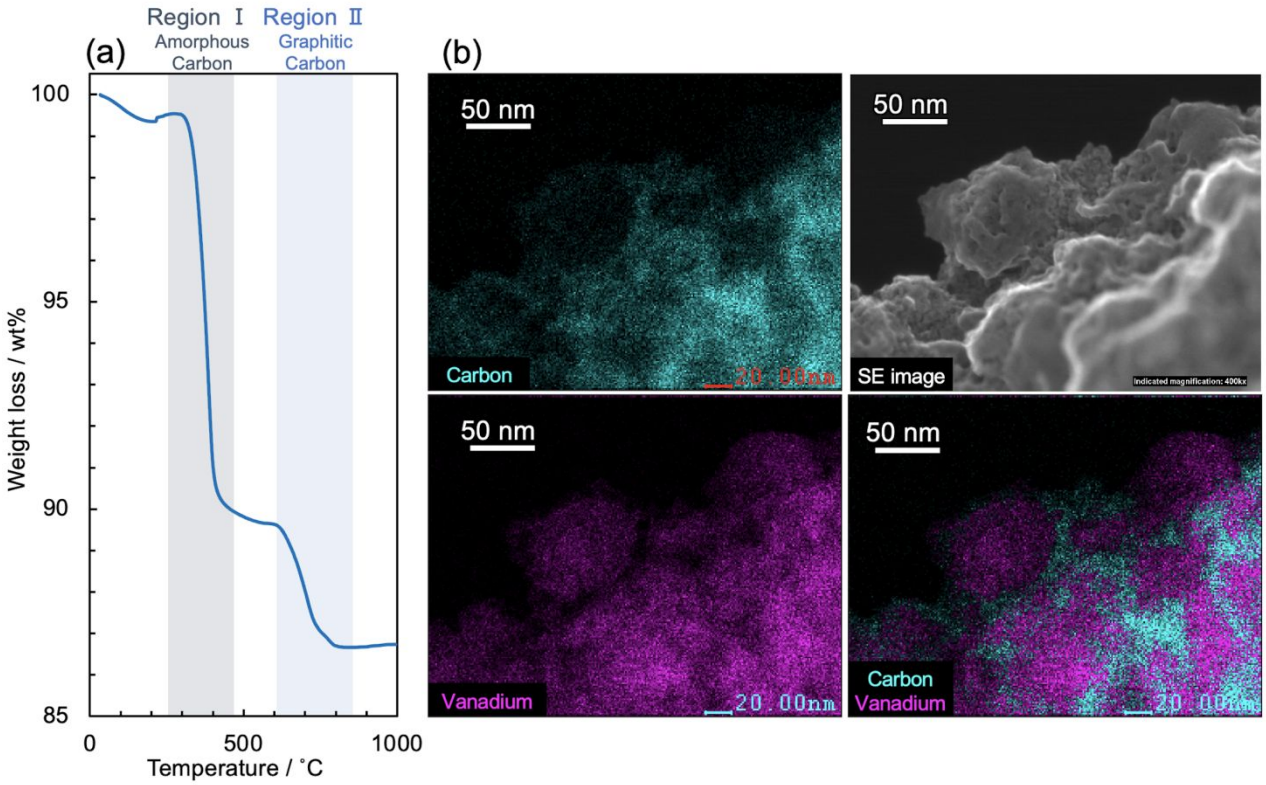

Figure 4. Characterization for the carbonaceous materials in the γ-LVSiO/C sample using (a) thermogravimetric (TG) measurement and (b) HR-STEM observation focusing on INNER PARTICLES (as shown in Figure 3). (a) TG curves for the γ-LVSiO/C clearly demonstrate that two-steps-weight loss between 250–450 °C (Region I) and 600–850 °C (Region II), corresponding to the combustion of amorphous and graphitic carbon, respectively. (b) EDS elemental maps of carbon, vanadium, and carbon/vanadium are also shown for the same region of the SE image. The comparison of the Secondary electron (SE) image with the elemental map (Carbon + Vanadium) clearly suggest that γ-LVSiO nanoparticles (50 nm or less) are interconnected with continuously filled carbon network. As shown in Figure S5, incidentally, the other elements (Si and O) are in the same way as the V distribution, indicative of the existence of the γ-LVSiO crystals which are completely separated by connecting carbon phase.

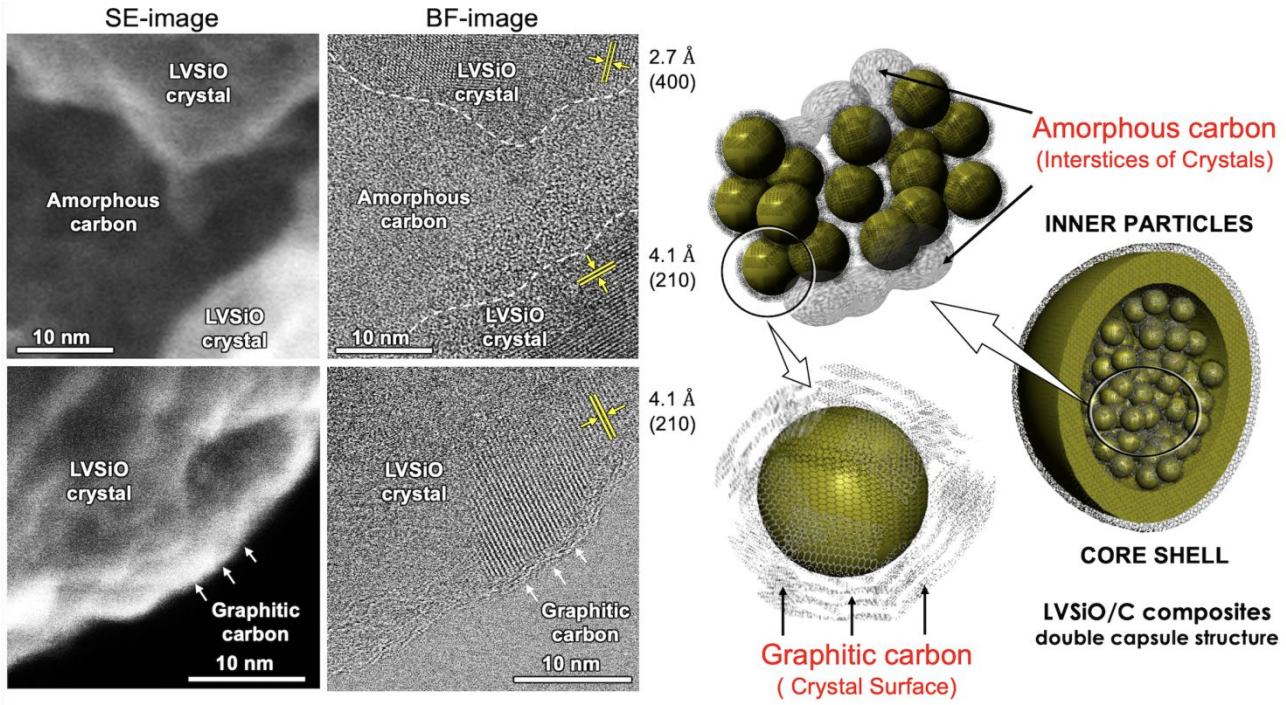

Figure 5. SE and Bright-field (BF) STEM images for the γ-LVSiO/C sample (as shown in Figure 2) focusing on the INNER PARTICLES in the core/shell architecture. The SE image (upper) together with the respective BF image clearly indicates that disordered amorphous carbon fills the interstices among the γ-LVSiO crystallites, as illustrated in the right side of the STEM images (upper). The crystallites have clear lattice fringes of d = 2.7 and 4.1 Å, corresponding to (400) and (210) planes of γ-LVSiO, respectively. On the other hand, the set of SE (lower) and BF (lower)-images displays the existence of another carbon which is very likely graphitic carbon (d = *ca.* 3.6 Å) with 2–4 stacked layers exactly placed the edge of the γ-LVSiO crystallites (as illustrated beside the STEM images (lower)).

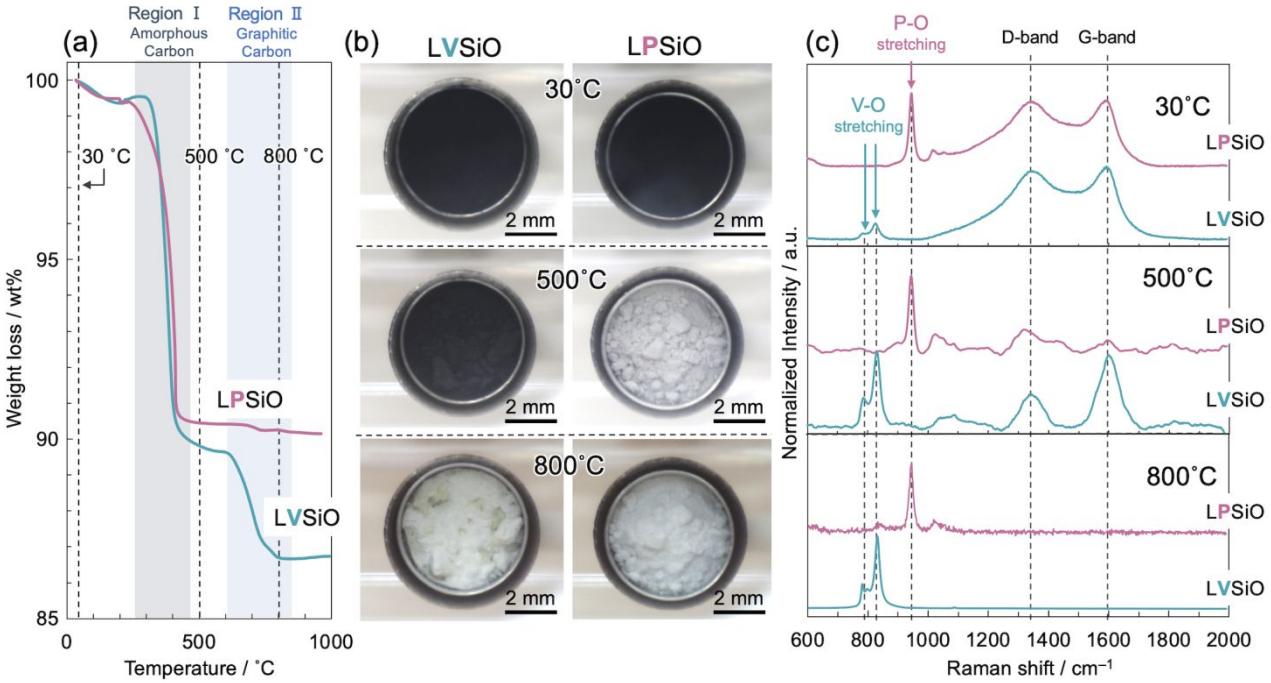

Figure 6. (a) TG curve for the γ-LVSiO/C clearly shows the two-steps-weight loss between 250–450 °C (Region I) and 600–850 °C (Region II), corresponding to the combustion of amorphous and graphitic carbon, respectively, while γ-LPSiO/C has only amorphous carbon loss. (b) Recorded photographs during TG measurements at 30, 500, and 800 °C indicate that the sample color of γ-LVSiO/C and γ-LPSiO/C changes from black (carbon) to white (original particles). The γ-LPSiO sample at 500 °C shows white color, where γ-LVSiO/C maintains black color derived from graphitic carbon. (c) Raman spectra of γ-LVSiO/C and γ-LPSiO/C after cooling down from 30, 500, and 800 °C reveal the crystallinity of the residual carbon from D-band and G-band peaks observed at 1350 cm^{-1} and 1590 cm^{-1} (the G/D ratios are tabulated in Table 2). Before heating up (30 °C), large peaks of carbon with high I_D/I_G ratios are found for both samples, indicative of the existence of the disordered phase. After combustion of the amorphous carbon (500 °C), the γ-LVSiO spectra shows low I_D/I_G ratio of graphitized phase, beside of the weak carbon peaks in the γ-LPSiO sample. All carbon peaks are completely disappeared at 800 °C.

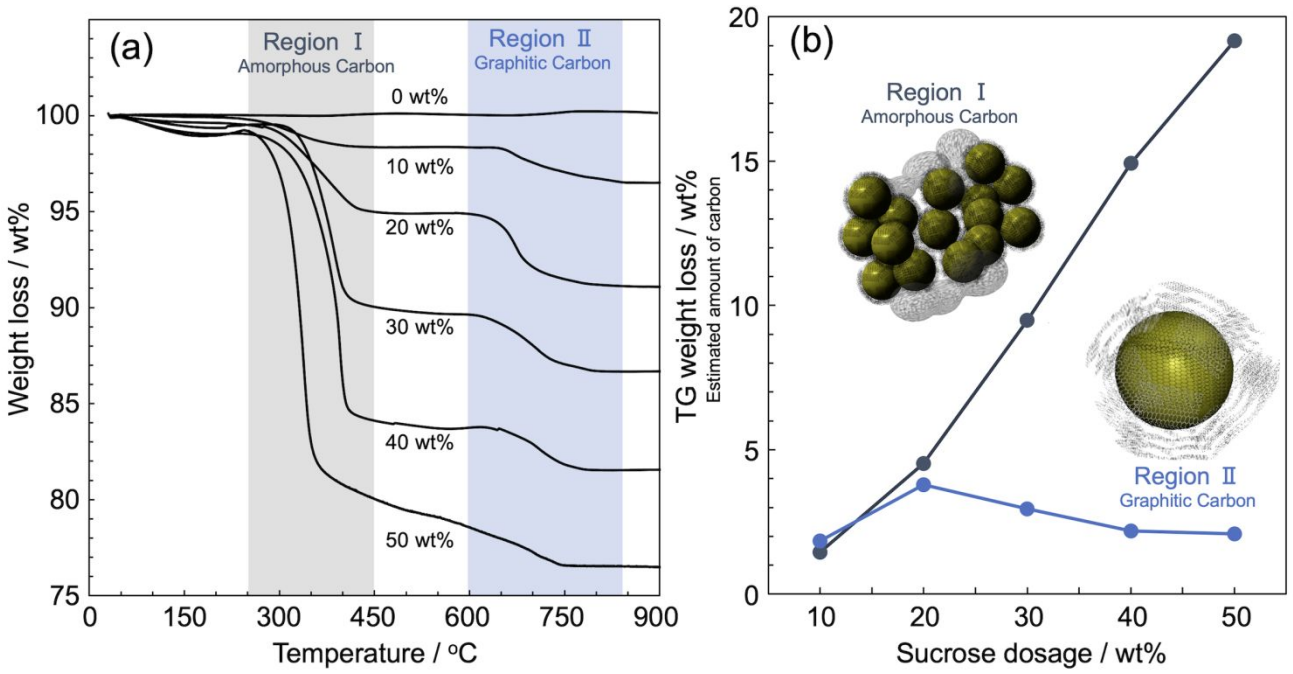

Figure 7. (a) TG curves for the γ-LVSiO/C composites synthesized from six types of feed solutions with different sucrose dosage in concentration of 0–50 wt%. All TG measurements were performed at a sweep rate of 5 °C min^{-1} under a synthetic airflow of 20% O_2 + 80% N_2. Weight losses are observed in the range of 250–450 °C (Region I) and 600–850 °C (Region II), corresponding to combustion of the amorphous and graphitic carbon, respectively, while Suc. 0 wt% exhibits no obvious weight losses. (b) Estimated amount of amorphous and graphitic carbon from the TG weight loss for the γ-LVSiO/C composites as a function of the sucrose dosage. With increase in sucrose concentration, amorphous carbon amount increases proportionally, while graphitic carbon is almost constant.

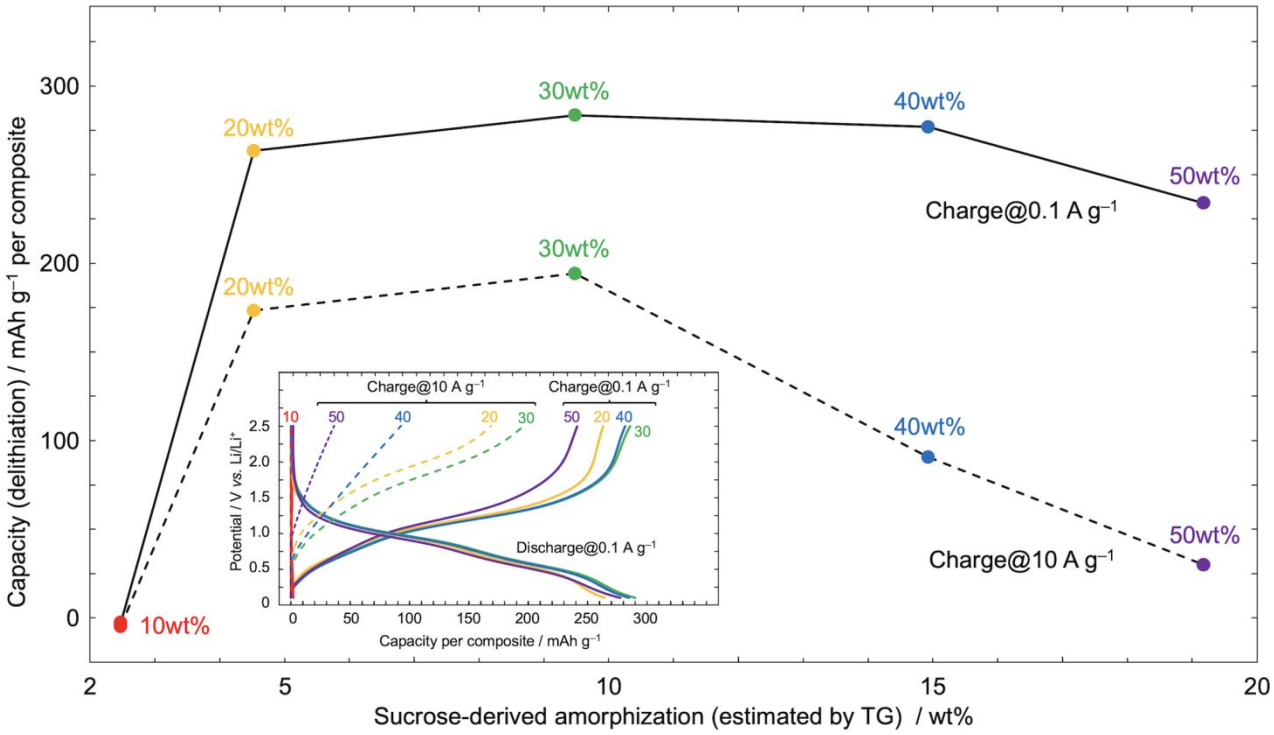

Figure 8. The correlation between rate performance and amorphous carbon amount (estimated by TG in Figure 7) for the γ-LVSiO/C. The rate performance test was performed using a half-cell consisting of Li/1 M $LiPF_6$ EC + DEC (vol 1:1)/spray-dried γ-LVSiO/C (synthesized from different sucrose dosage of 10–50wt%) at different charge current density of low-rate (0.1 A g^{-1}) and high-rate (10 A g^{-1}) with constant discharge density (0.1 A g^{-1}). The corresponding potential profiles are shown in the inset. The rate performances are clearly correlated to the amount of amorphous carbon. The capacity retention at 10 A g^{-1} is maximized at 9.8 wt% of amorphous carbon (30 wt% of sucrose dosage), which deteriorates with increase/decrease in amount of the amorphous carbon.

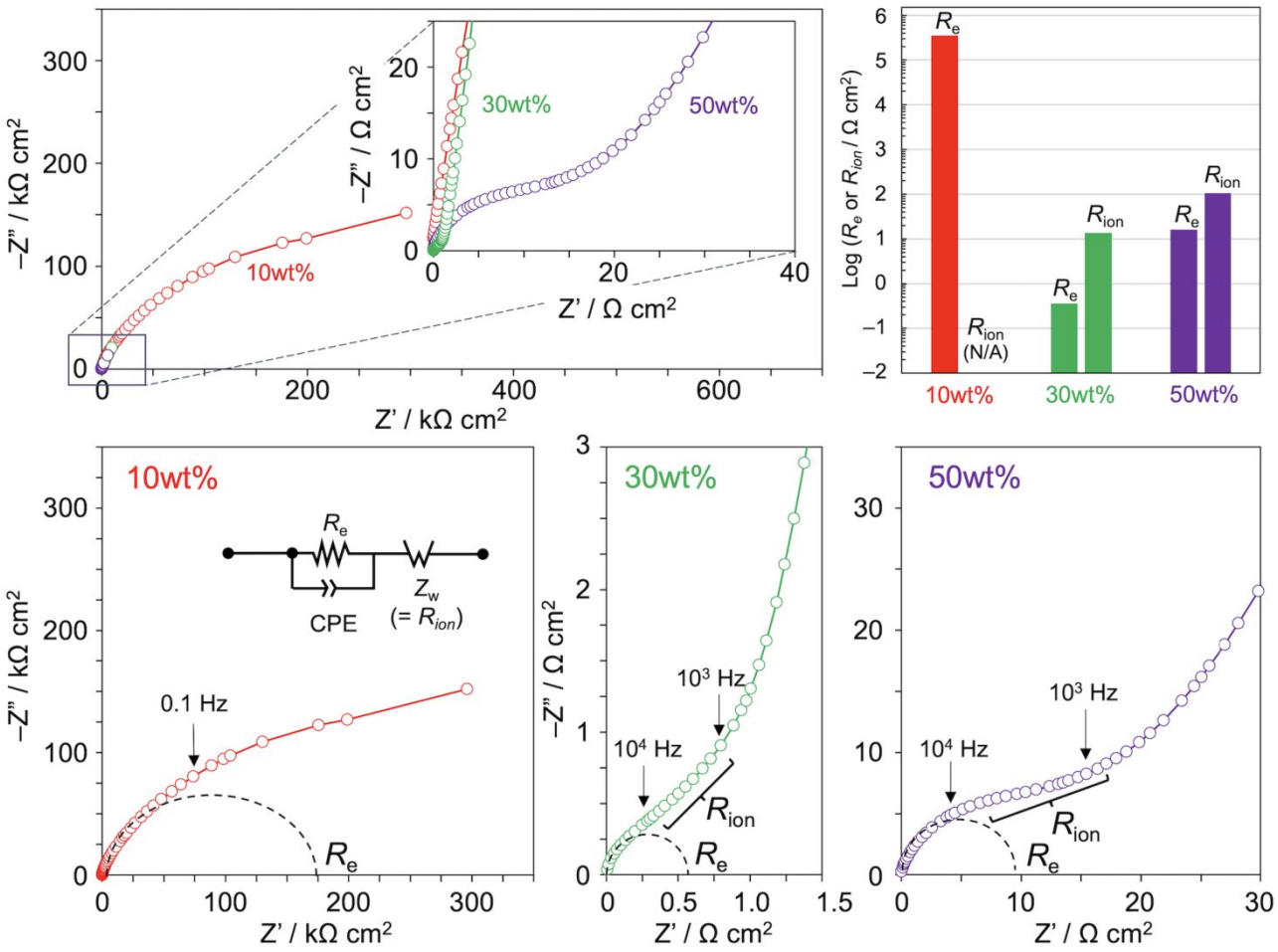

Figure 9. Nyquist plots for the γ-LVSiO/C (synthesized from 10, 30, and 50 wt% of sucrose dosage), whose solution resistances have been subtracted to align the intersection with the horizontal axis at zero point. All measurements were conducted by using a symmetric blocking cell at 0% of state of charge. The corresponding equivalent circuit is shown in the inset. Sucrose 10 wt% sample shows a huge semicircle derived from electronic resistance of the grain boundary (R_e). Sucrose 30 and 50 wt% samples exhibit the collapsed semicircle (high frequency: *ca.* 10^4 Hz) and inclined liner component (low frequency: *ca.* 10^3 Hz), corresponding to the resistance of R_e and ionic resistance of the electrolyte diffusion (R_{ion}). Estimated resistances (summarized in a bar graph) are minimized in the sucrose 30 wt%.

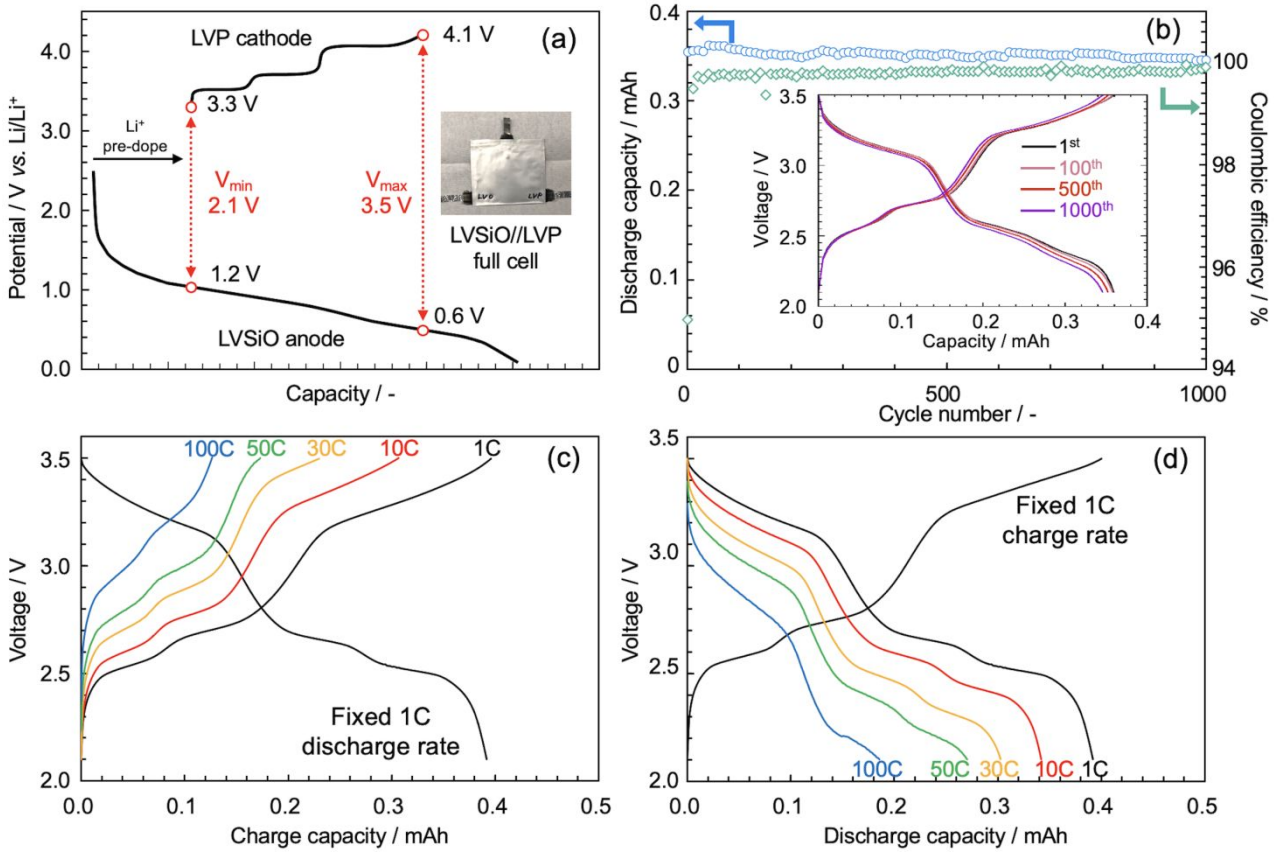

Figure 10. Full cell performances of 0.4 mAh-class laminate-type cells composed of (γ-LVSiO/C of Suc. 30 wt%)/1 M $LiBF_4$ EC + DEC (vol 1:1)/(uc-$Li_3V_2(PO_4)_3$/MWCNT) operated in a voltage range of 2.1–3.5 V. (a) Potential profiles of γ-LVSiO anode and LVP cathode in the full cell configuration, where the operation voltage and N/P ratio are optimized by Li^+ pre-dope for long cyclability, as previously reported [62]. (b) Plots of capacity and coulombic efficiency during cyclability tests at a constant charge-discharge current density of 10C. (Inset) Corresponding voltage profiles at the 1st, 100th, 500th, and 1000th cycles (c) Voltage profiles at different charge currents of 1, 10, 30, 50, 100 C (1C = 0.4 mA) with a fixed discharge current of 1C. (d) Voltage profiles at different discharge currents with a fixed charge current of 1C.